

Generalized 3D and 4D Motion Compensated Whole-body PET Image Reconstruction Employing Nested EM Deconvolution

Nicolas A. Karakatsanis,
Habib Zaidi

Division of Nuclear Medicine
University of Geneva
Geneva, Switzerland
nikolaos.karakatsanis@unige.ch

Charalampos Tsoumpas
Department of Medical Physics
University of Leeds
Leeds, United Kingdom

Habib Zaidi
Department of Nuclear Medicine and
Molecular Imaging
University of Groningen,
Groningen, Netherlands

Abstract—Whole-body dynamic and parametric PET imaging has recently gained increased interest as a clinically feasible truly quantitative imaging solution for enhanced tumor detectability and treatment response monitoring in oncology. However, in comparison to static scans, dynamic PET acquisitions are longer, especially when extended to large axial field-of-view whole-body imaging, increasing the probability of voluntary (bulk) body motion. In this study we propose a generalized and novel motion-compensated PET image reconstruction (MCIR) framework to recover resolution from realistic motion-contaminated static (3D), dynamic (4D) and parametric PET images even without the need for gated acquisitions. The proposed algorithm has been designed for both single-bed and whole-body static and dynamic PET scans. It has been implemented in fully 3D space on STIR open-source platform by utilizing the concept of optimization transfer to efficiently compensate for motion at each tomographic expectation-maximization (EM) update through a nested Richardson-Lucy EM iterative deconvolution algorithm. The performance of the method, referred as nested RL-MCIR reconstruction, was evaluated on realistic 4D simulated anthropomorphic digital XCAT phantom data acquired with a clinically feasible whole-body dynamic PET protocol and contaminated with measured non-rigid motion from MRI scans of real human volunteers at multiple dynamic frames. Furthermore, in order to assess the impact of our method in whole-body PET parametric imaging, the reconstructed motion-corrected dynamic PET images were fitted with a multi-bed Patlak graphical analysis method to produce metabolic uptake rate (K_i parameter in Patlak model) images of highly quantitative value. Our quantitative Contrast-to-Noise (CNR) and noise vs. bias trade-off analysis results suggest considerable resolution enhancement in both dynamic and parametric motion-degraded whole-body PET images after applying nested RL-MCIR method, without amplification of noise.

Keywords—PET; dynamic; 4D; whole-body; Patlak; EM; deconvolution; Richardson-Lucy; motion; intra-frame

I. INTRODUCTION

Oncology has benefited considerably by the advent of clinical Positron Emission Tomography (PET) imaging. Until recently, the established surrogate of standardized uptake value (SUV) has been employed to evaluate the metabolic activity concentration of the administered radioactive tracer in normal

and pathological tissues. However, SUV measurements are dependent on time and tracer concentration in blood plasma (input function), thus, their evaluation may not be sufficient for quantitative tasks, such as tumor therapy response assessments [1]. On the contrary, dynamic PET imaging, involving multiple static acquisitions over time for a single bed position, can allow for tracking of the activity distribution from injection time. The four-dimensional (4D) collected data can be further analyzed, utilizing graphical or compartmental kinetic models, to estimate physiological parameters of interest, such as the tracer uptake rate K_i . By efficiently complementing SUV with parametric measurements, accuracy in the diagnostic, prognostic and treatment response assessments can be enhanced. Until now, dynamic PET acquisitions have been limited to the axial field-of-view (FOV) of single beds and, thus, have not been translated to the clinic, where whole-body imaging is necessary for evaluation of disease spread.

Recently, we proposed a clinically feasible whole-body FDG PET parametric imaging framework capable of delivering highly quantitative multi-bed parametric images [1]. However, the presented protocol requires relatively long acquisitions of ~30-40min and short dynamic frames of 30-45sec. The former attribute can considerably increase the probability for non-rigid voluntary body (bulk) motion within each frame (intra-frame motion) as well as across the frames (inter-frame motion), while the latter increases noise levels. Thus, the quantitative accuracy (bias/resolution) and precision (noise) in both dynamic and parametric images may be degraded [2].

The majority of existing motion compensated PET image reconstruction methods for non-brain data focus mainly on respiratory and cardiac motion, neglecting voluntary body motion, while they rely on gating of the PET data, assuming sufficient statistics at each gate [3,4]. However, the unpredictability of voluntary body motion, when combined with the dynamic nature of acquisition and the need for short frames, present a challenge in properly gating each dynamic frame based on tracked motion, even when motion estimation performance itself is considered satisfactory [5]. For instance, a higher number of irregular non-rigid bulk motions may occur within certain dynamic PET frames. Thus, those frames may be time-segmented into gates of not only very low but also highly

unbalanced number of counts. Therefore, a non-gated motion compensated reconstruction algorithm would constitute a more feasible and practical solution to the problem of motion correction in dynamic and parametric PET imaging, particularly when multiple beds are involved.

Moreover, in dynamic PET imaging voluntary body movements is often a major motion component due to longer acquisitions. Especially for whole-body dynamic acquisitions, where the total scan duration is longer, the probability of extensive body motion becomes considerable. In addition, voluntary body motion, in contrast to nearly periodic respiratory and cardiac motion, is relatively more irregular increasing the likelihood of inter-frame misalignments, thus, particularly affecting parametric images. Therefore, the challenge of compensation for voluntary body motion becomes highly important in dynamic and parametric PET imaging.

In this study, we present a *generalized* maximum-likelihood expectation-maximization (ML-EM) dynamic PET image reconstruction framework incorporating motion deconvolution capabilities to produce highly quantitative accuracy and precise motion-compensated whole-body PET images from non-gated data. The proposed nested ML-EM reconstruction algorithm can model any type of motion transformation and is applicable to both static and dynamic whole-body PET data with or without gates, thanks to a generalized motion model that relies on the accuracy in the estimated MVFs of the motion transformations. It employs the concept of optimization transfer to define appropriate ML-EM surrogate objective functions at each iteration step, allowing for the efficient decoupling of the slower EM tomographic estimation problem in the projection space from the faster motion EM deconvolution process in the image space. A Richardson-Lucy EM (RL-EM) iterative deconvolution algorithm is nested within each iteration step of the tomographic ML-EM algorithm to compensate for the tracked non-rigid motion at each dynamic frame, alleviating the need for gated acquisition. Finally, the presented method has been implemented and validated in fully 3D space on the Software for Tomographic Image Reconstruction (STIR v3.0) open-source platform [6], an object-oriented C++ reconstruction library, and is scheduled for public open-source release.

II. THEORY

A. Generalized motion model in image space

Each non-rigid 3D motion transformation can be expressed in the form of a set of three 3D motion vector fields (MVFs), each along one of the three Cartesian coordinate directions x, y and z. Subsequently, a warping operator can transform an original emission (e.g. PET) or attenuation (e.g. attenuation map derived from CT or MRI) image according to the motion described in the MVFs. When gated acquisition is possible, the MVF for each gated image can be estimated using advanced registration techniques [7]; however, for irregular and unpredictable types of motion, such as voluntary body motion, gated acquisition becomes challenging without list mode capabilities, even when ideal motion tracking is assumed.

The presented method can potentially model any type of combined (e.g. respiratory + cardiac + bulk + rigid) motion,

limited only by the spatial and time resolution of the tracked motion data. In this study, we are focusing on the motion correction problem itself assuming that motion estimation is reasonably accurate. The forward motion model employed here considers each motion-contaminated image as a time-weighted average of a set of motion-transformed/warped images:

$$m_{jt}(\mathbf{x}_t) = \sum_{s \in \mathcal{S}_t} c_{st} W_{j_0 \rightarrow j_s}^s(\mathbf{x}_t) \quad (1)$$

Notation:

- $W_{j_0 \rightarrow j_s}^s$ is the forward motion warping/transform operator from voxel j_0 of the original image space to voxel j_s of the motion-transformed image space for a particular s transformation,
- $\mathbf{x}_t \equiv [x_{j_0 t}]_{j_0=1}^{n_j}$ and $\mathbf{m}_t \equiv [m_{jt}]_{j=1}^{n_j}$ are the motion-corrected and motion-contaminated images of dynamic frame t , respectively. Both images are comprised of n_j voxels in total. Note that the overall weighted averaging operation resulted in a new motion-blurred image space, denoted with voxel index j , for the \mathbf{m}_t images. The image vectors can represent either reconstructed PET or CT- or MRI-derived attenuation images. For notation simplicity we assume that all types of images are of the same dimensions in this study,
- \mathcal{S}_t is the subset of motion transformations occurring during frame t and
- c_{st} is the respective time-weighting factor, defined as the time fraction relative to the duration of frame t , for which the $s \in \mathcal{S}_t$ motion transformation holds.

The overall effect of this time-weighted averaging operation is the introduction of motion-induced blurring in each of the original motion-free dynamic PET images, similar with the effect of convolving with an image-based kernel and, thus, the presented approach has analogies with image-based point spread function (PSF) or resolution recovery modeling.

B. Integrated modeling of motion within ML-EM dynamic PET image reconstruction (integrated RL MCIR)

We assume, throughout this study, a PET system with n_i detector pair bins in fully 3D mode and a reconstruction of n_t dynamic images of n_j voxels each. Initially, let us consider the conventional approach of completely integrating the previous motion model to the PET ML-EM reconstruction framework, referenced in the rest of the text as *integrated RL MCIR* algorithm. After adding the image-based motion modeling term $m_{jt}(\mathbf{x}_t)$ (eq. 1) into the ML-EM image estimation algorithm, the EM forward projection process can be described as follows:

$$\bar{y}_{it}(\mathbf{x}_t) = \sum_j p_{ij}^t m_{jt}(\mathbf{x}_t) + \bar{r}_{it} \quad (2)$$

Notation:

- $\bar{\mathbf{Y}} \equiv [\bar{y}_{it}]_{i,t=1}^{n_i, n_t}$ are the expected projection data acquired during frame t ,

- $\mathbf{X} \equiv [\mathbf{x}_t]_{t=1}^{n_t}$ are the unknown dynamic motion-compensated images to be estimated,
- $\bar{\mathbf{R}} \equiv [\bar{r}_{it}]_{i,t=1}^{n_i, n_t}$ are the expectation of scattered and random events at each dynamic frame t and
- $\mathbf{P}^t \equiv [p_{ij}^t]_{i,j=1}^{n_i, n_j}$ is the system response matrix at frame t with each element p_{ij}^t denoting the probability of an annihilation event occurring in voxel j being detected in sinogram bin i during frame t .

Dynamic PET ML-EM reconstruction schemes aim at maximizing the Poisson log-likelihood of the measured dynamic projection measurements $\mathbf{Y} \equiv [y_{it}]_{i,t=1}^{n_i, n_t}$, given the estimated dynamic images \mathbf{X} , with $\mathbf{y}_t \equiv [y_{it}]_{i=1}^{n_i}$ denoting the measured projection data for t time frame:

$$L(\mathbf{Y}|\mathbf{X}) = \sum_t \sum_i y_{it} \log \bar{y}_{it}(\mathbf{x}_t) - \bar{y}_{it}(\mathbf{x}_t) \quad (3)$$

$$L_t(\mathbf{y}_t|\mathbf{x}_t) = \sum_i y_{it} \log \bar{y}_{it}(\mathbf{x}_t) - \bar{y}_{it}(\mathbf{x}_t) \quad (4)$$

A term independent of \mathbf{x}_t is neglected from both equations above, as it does not participate in the optimization w.r.t. \mathbf{x}_t . The ML solutions, for each frame t , maximizing both log-likelihoods (eq. 3 and 4) are the following:

$$\hat{\mathbf{x}}_t = \operatorname{argmax}_{\mathbf{x}_t} L_t(\mathbf{y}_t|\mathbf{x}_t) \quad (5)$$

In this study we are focusing only on ML solutions to mainly demonstrate the concept of nested EM motion deconvolution for the standard ML-EM reconstruction framework. However the presented methods can be easily extended to *maximum-a-posteriori* (MAP) reconstructions by efficiently accounting for a prior estimate in eq. 3 and 4 using the one-step-late (OSL) approach. When applying the ML-EM algorithm, the following *conventional* EM update equation is derived for each t frame, theoretically converging to a motion-compensated dynamic image of maximum log-likelihood:

$$\begin{aligned} x_{j_0 t}^{n+1} &= \frac{x_{j_0 t}^n}{\sum_{s \in S_t} c_{st} W_{j_s \rightarrow j_0}^s \{\mathbf{1}\} \sum_i p_{ijt}} \\ &\times \sum_{s \in S_t} c_{st} W_{j_s \rightarrow j_0}^s \left\{ \sum_i p_{ijt} \frac{y_{it}}{\bar{y}_{it}(\mathbf{x}_t^n)} \right\} \end{aligned} \quad (6)$$

The integration of motion modeling within the forward and backward tomographic projection operations effectively adds to the algorithm the extra task of solving for an image deconvolution problem simultaneously with the tomographic problem. As the spatial correlations among the voxels of the reconstructed image updates are enhanced with the addition of motion modeling, the EM algorithm now requires more iteration steps to converge to an ML solution. However, the major contribution to the computational cost per iteration originates from the tomographic forward- and back-projection operations, while the motion deconvolution is much faster.

Therefore, one of the drawbacks of the conventional integrated RL-MCIR reconstruction is the slower convergence,

in terms of number of iterations required for convergence, which is expected due to the inherent nature of the ML-EM estimation problem. However, this would not have been a serious concern, had the computational cost been limited, as the primary concern in practice for convergence is the total computational time. In fact, the major limitation of the integrated RL-MCIR algorithm is, beside the need for larger number of iterations, the considerably higher computational cost per iteration, due to coupling of the faster image-based deconvolution process together with the considerably slower tomographic updates of the n_t dynamic images.

C. Nested RL-EM motion deconvolution within ML-EM dynamic PET image reconstruction (nested RL-MCIR)

In this section, a nested motion-compensated PET image reconstruction algorithm is presented capable of similarly compensating for generalized motion in non-gated frames through motion RL-EM deconvolution. However, in this approach the slow tomographic EM estimation problem is efficiently decoupled from the faster image-based motion EM deconvolution process at every iteration step. We refer to this new ML-EM algorithm as *nested RL-MCIR*. The decoupling is achieved by decomposing each originally integrated ML-EM iteration step into a single time-consuming projection-based tomographic EM update step and multiple *nested* image-based fast EM deconvolution updates to accelerate convergence. Nested RL-MCIR can converge faster thanks to its ability to perform multiple nested EM deconvolution updates within each global iteration step. Although the computational cost for each nested update dramatically reduces, allowing for faster motion EM deconvolution, the respective cost for each global iteration step is slightly higher in nested RL-MCIR. However, the considerable benefit from performing multiple nested motion deconvolution iterations within a single tomographic iteration allows for significantly fewer iterations to convergence and, thus, for reduction in noise propagation and computational time/cost.

The principles of optimization transfer [8] are employed to construct, at each iteration step n , a surrogate objective function for which optimization is simplified, while ensuring convergence to the global ML solution of Eq. (5):

$$Q_t(\mathbf{x}_t|\mathbf{x}_t^n) = \sum_j \left(\sum_i p_{ij} \right) m_{jt}^{em,n} \log m_{jt}(\mathbf{x}_t) - m_{jt}(\mathbf{x}_t) \quad (7)$$

The constructed image-based surrogate objective functions, defined for each t frame, express the log-likelihood of an estimated image frame \mathbf{x}_t , given the current update \mathbf{x}_t^n of that frame. Thus, the maximization problem of the original log-likelihood objective function $L_t(\mathbf{y}_t|\mathbf{x}_t)$ is effectively transferred, at each iteration step n , into the maximization of the current surrogate objective function $Q_t(\mathbf{x}_t|\mathbf{x}_t^n)$:

$$\mathbf{x}_t^{n+1} = \operatorname{argmax}_{\mathbf{x}_t} Q_t(\mathbf{x}_t|\mathbf{x}_t^n) \quad (8)$$

The objective functions in Eqs. (7) and (8) and, thus, the optimization problem for each t frame, differs at every global iteration step, thus, producing every time a new ML solution \mathbf{x}_t^n , that should in turn converge to the global ML solution $\hat{\mathbf{x}}_t$. The concept of optimization transfer for the nested RL MCIR

approach is illustrated in Fig. 1. The global convergence of the ML-EM problem is guaranteed as the surrogate objective functions $Q_t(\mathbf{x}_t|\mathbf{x}_t^n)$ satisfy the constraints shown in Fig. 1 [8].

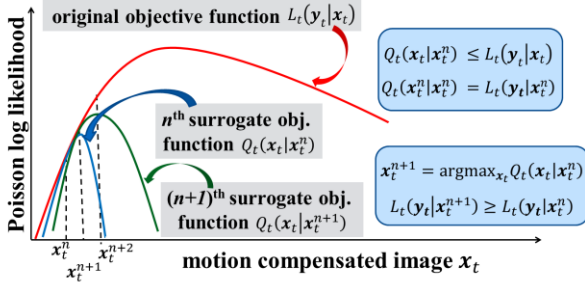


Fig. 1. Graphical illustration of the optimization transfer concept and the constraints that the constructed surrogate objective functions should satisfy at every iteration step. The maximization problem of the original objective function (red) is transferred to the maximization of the less complex image-based surrogate objective functions at n (blue) and $n+1$ (green) iteration steps.

Thus, a nested ML-EM algorithm is employed to produce the ML solutions of eq. 5 and 8. At global iteration step $n + 1$, initially, an intermediate motion-contaminated image estimate $\mathbf{m}_t^{em,n}$ is derived, at each t frame, using the measured projection data y_{it} as reference:

$$m_{jt}^{em,n} = \frac{m_{jt}(\mathbf{x}_t^n)}{\sum_i p_{ijt}} \sum_i p_{ijt} \frac{y_{it}}{y_{it}(\mathbf{x}_t^n)} \quad (9)$$

Subsequently, a *nested* Richardson-Lucy EM update equation is employed to iteratively deconvolve the image and estimate after $k = 1, \dots, n_k$ nested iterations, the next global motion-free image \mathbf{x}_t^{n+1} , utilizing the previously estimated motion-contaminated image $\mathbf{m}_t^{em,n}$ as a reference:

$$x_{j_0 t}^{n,k+1} = \frac{x_{j_0 t}^{n,k}}{\sum_{s \in S_t} c_{st} W_{j_s \rightarrow j_0}^s \{1\}} \sum_{s \in S_t} c_{st} W_{j_s \rightarrow j_0}^s \left\{ \frac{\mathbf{m}_t^{em,n}}{\mathbf{m}_t(\mathbf{x}_t^{n,k})} \right\} \quad (10)$$

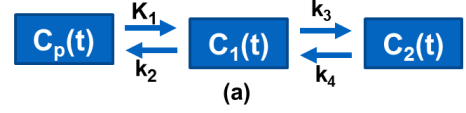
After all n_k nested iterations, the derived \mathbf{x}_t^{n,n_k+1} image update is considered the next global ML motion-corrected image update \mathbf{x}_t^{n+1} that will be used as initializer for the subsequent global iteration step $n + 2$. Thus, using a voxel-based equation notation, we have: $x_{jt}^{n,1} = x_{jt}^n$, $x_{jt}^{n,2} = x_{jt}^{n,n_k+1}$.

The iterative RL deconvolution scheme had been previously evaluated for motion correction with promising results, but only for rigid brain motion and exclusively as a post-reconstruction process, i.e. not within the ML-EM framework, resulting in high amplification of noise with deconvolution iterations, due to the indirect nature of motion correction [9,10]. However, both the integrated and nested RL MCIR algorithms enable, at each iteration step, the EM motion deconvolution directly from projection data, where the noise follows the well-defined Poisson distribution which can be more accurately modeled. Thus, RL-MCIR algorithms can potentially allow for more effective noise suppression in the motion-compensated images, compared to post-reconstruction RL schemes, a feature which is very important for the high noise levels usually present in low-count or dynamic PET data, especially for whole-body dynamic acquisitions [2].

III. METHODS

A. Generation of realistic kinetic 4D simulated image data

The performance of the proposed motion-compensated nested ML-EM PET dynamic image reconstruction method is evaluated on realistic 4D simulated emission and attenuation data acquired according to our previously proposed clinically feasible whole-body dynamic acquisition PET protocol to reproduce as close as possible the clinical challenges associated with this protocol in terms of noise levels, types of motion as well as sampling of the time activity curves (TACs) [1,11].



Regions	K_1	k_2	k_3	k_4	V_p
Normal Liver	0.864	0.981	0.005	0.016	-
Liver Tumor	0.243	0.78	0.1	0	-
Normal Lung	0.108	0.735	0.016	0.013	0.017
Lung Tumor	0.044	0.231	1.149	0.259	-
Myocardium	0.6	1.2	0.1	0.001	-

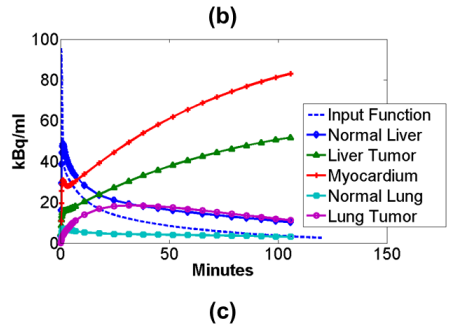


Fig. 2. (a) The standard fully compartmental FDG-PET tracer kinetic model was employed in this study. It consists of the $C_p(t)$ input function compartment, as well as the tissue compartments for free-tracer $C_1(t)$ and metabolized FDG $C_2(t)$ concentration over post-injection time t . (b) the k -parameter table reviewed from literature and (c) the TACs for multiple normal and tumor regions belonging to a cardiac bed FOV.

The standard kinetic model for fluorodeoxyglucose (FDG) tracer, i.e. a 2-compartment 4-kinetic parameter compartmental model (Fig. 2a), and the Feng input function model were employed for the production of the simulated noise-free TACs for a range of normal tissues and tumors in the torso region (Fig. 2c) [1]. The kinetic parameter values, tabulated in Fig. 2b, were acquired from literature review of recent clinical dynamic PET studies [1,2]. Subsequently, the noise-free TACs were assigned to the respective region voxels of the anthropomorphic digital XCAT human torso phantom [12], limited to a Biograph mCT cardiac bed axial FOV, in order to generate realistic motion-free kinetic 4D XCAT phantom images. In addition, a single motion-free XCAT PET attenuation map was created.

B. Application of real human MRI-derived body motion

A series of real human body non-rigid and highly irregular motion transformations were applied to each dynamic cardiac PET image frame of the XCAT phantom. The initial motion-transformed 3D XCAT images were provided from a recently published dataset, which was created and validated by Dr. Arda

König from human volunteer MRI scans mimicking characteristic bulk and respiratory motions [13]. The exercised natural 3D motion transformations were tracked thanks to reflective markers, properly positioned on body surface, and 3D stereo optical imaging tracking techniques [13]. Multiple combinations from a range of basic voluntary body motions were applied in different combinations over the initial motion-free dynamic frames, resulting in a total of 30 different non-rigid transformations randomly distributed across the 6 cardiac frames. The following five types of body motions were randomly combined: axial slide (rigid motion), lateral torso bend, shoulder twist, shoulder stretch and side roll [13].

Initially, the five basic human motion transformations above were applied to XCAT to generate five motion-transformed editions for each frame. Then a hierarchical local affine registration method [6] was utilized to estimate, for each of the five motion transformations of each frame, three MVFs, each corresponding to the x, y and z Cartesian directions. The resulting $6 \times 5 \times 3 = 90$ MVFs were averaged across frames to produce $5 \times 3 = 15$ averaged MVFs of higher precision for each of the basic five motions. Later, the 5 sets of MVFs were randomly combined, at each x, y and z direction, to create 25 new sets of MVFs, i.e. $n_s = 30$ MVF sets were created in the end. One characteristic set of MVFs is shown in Fig. 3.

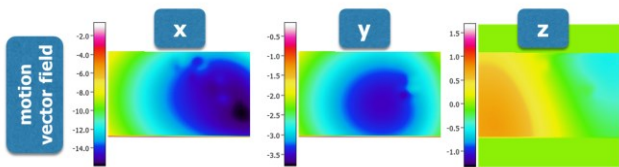


Fig. 3. A characteristic example of x, y and z 3D MVFs corresponding to one of the 30 motion transformations applied to the simulated 4D data. Each transformation, represented by a set of 3 3D MVFs, is a combination of the five basic transformations estimated from the initial XCAT dataset.

Subsequently, the 30 motion transformations were randomly grouped into 6 motion sets, each denoted as \mathbf{s}_t , $t = 1, \dots, 6$. The assignments of motions to dynamic frames were identical between emission and attenuation frames. Then, each motion transformation s was applied, through the warping operation $W_{j_0 \rightarrow j_s}^s$, $s \in \mathbf{s}_t$, to its corresponding motion-free frame \mathbf{x}_t , as indicated by its group \mathbf{s}_t , to produce 30 noise-free motion-transformed 3D PET emission images \mathbf{d}_s . In addition, the same set of transformations was also applied to the single XCAT attenuation image $\boldsymbol{\mu}_0$ to produce 30 motion-transformed PET attenuation images $\boldsymbol{\mu}_s$.

C. Simulation of 4D motion-contaminated projection PET emission, attenuation and parametric data

Initially, each motion-transformed attenuation PET image $\boldsymbol{\mu}_s$ was forward projected and the respective attenuation factor sinograms were calculated as: $\mathbf{a}_s = e^{-\text{fwdproj}(\boldsymbol{\mu}_s)}$, where “fwdproj” denotes the Biograph mCT (Siemens Healthcare) fully 3D analytic forward projection operation implemented in STIR [5]. Subsequently, each motion-transformed PET emission image \mathbf{d}_s was forward projected, followed by application of the respective attenuation factors \mathbf{a}_s in the projection space to produce the corresponding motion-

transformed attenuated noise-free emission projection data $\mathbf{e}_s = \mathbf{a}_s \circ \text{fwdproj}(\mathbf{d}_s)$ with “ \circ ” denoting a Hadamard or component-wise matrix product operation. Then, each motion-contaminated sinogram $\mathbf{y}_t = \sum_{s \in \mathbf{s}_t} c_{st} \mathbf{e}_s$ is calculated as the time-weighted average of the group of transformed sinograms \mathbf{e}_s , $s \in \mathbf{s}_t$, corresponding to a certain frame. For this proof of concept study scatter and random events were not added.

A total of 20 realizations of quantitative levels of Poisson noise were added to each simulated dynamic sinogram \mathbf{y}_t according to the current mean ^{18}F radioactivity of each frame, as determined by the reported sensitivity and dead time of the mCT scanner, the ^{18}F decay rate and the duration t_s of each frame. Later, the noise-free and noisy dynamic projections, without and with motion, were reconstructed using the standard ML-EM algorithm in STIR. The motion-contaminated dynamic projections were also reconstructed with our proposed nested RL-MCIR algorithm, as implemented in fully 3D within STIR v3.0. The attenuation correction factors (ACFs) sinograms $\bar{\mathbf{a}}_t$ were derived by time-weighted averaging the motion-transformed ACF sinograms \mathbf{a}_s , $s \in \mathbf{s}_t$, i.e. $\bar{\mathbf{a}}_t = \sum_{s \in \mathbf{s}_t} c_{st} \mathbf{a}_s$. We consider the derived map in order to minimize any mismatches between emission and attenuation in each frame.

Finally, all reconstructed whole-body dynamic frames and the measured input function $b_t = b(\tau_t)$ at mid-frame times τ_t were fitted with our proposed multi-bed version of Patlak linear graphical analysis method [1],[2] to estimate at each voxel the physiologic parameters of tracer uptake rate K_i and total blood volume distribution V : $x_{jt} = K_i \int_0^{\tau_t} b_t d\tau + V b_t$.

IV. RESULTS

The cardiac beds from the reconstructed dynamic and parametric whole-body PET images without and with noise are presented in Figs. 4 and 5, respectively. Similar results were obtained for the other beds. The impact of real voluntary human body motion is evident in both noise-free and noisy motion-contaminated dynamic and parametric images (2nd column). It is stronger for the parametric K_i Patlak images due to presence of considerable inter-frame motion. In addition, contrast-to-noise ratios and noise vs. bias trade-off performance for different ML-EM iterations are presented in Fig. 6. The application of the nested RL-MCIR method (10 nested iterations) partially recovers, without further amplifying noise, most of the resolution of the motion-free dynamic and parametric images with greater enhancements for the latter.

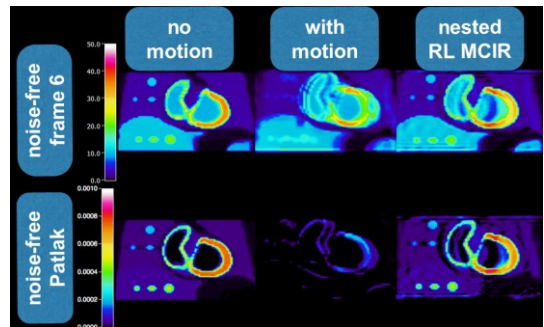


Fig. 4. Noise-free reconstructed (1st row) dynamic PET and (2nd row) Patlak K_i images. (1st column) without motion, (2nd column) with motion but no correction, and (3rd column) with motion but after applying nested RL MCIR.

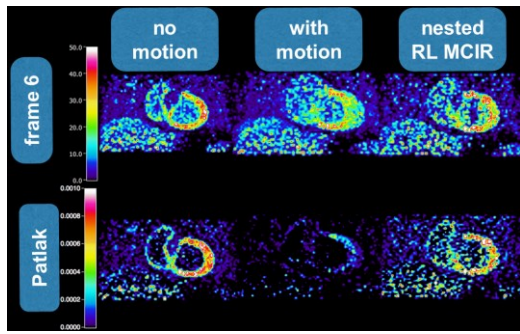


Fig. 5. Same type of datasets with Fig. 4 but after adding quantitative levels of Poisson noise on projection space for 45sec Biograph mCT PET frames

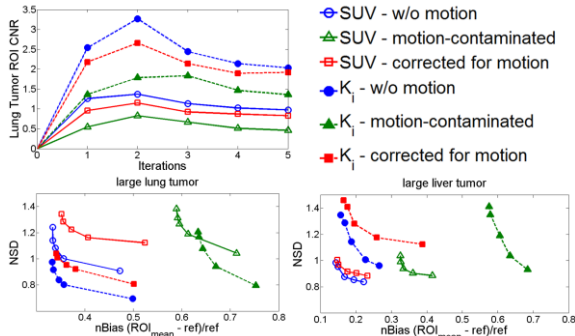


Fig. 6. (Top-left) Contrast-to-Noise ratios (CNRs) for lung tumor and (bottom row) noise vs. bias trade-off performance for lung and liver tumors.

V. DISCUSSION AND CONCLUSION

In this work, we are proposing a generalized motion-compensated ML-EM PET image reconstruction algorithm employing nested Richardson-Lucy EM motion deconvolution to efficiently recover the motion-degraded spatial resolution of non-gated PET images. The method is applicable to a) both static and dynamic data, b) single-bed and whole-body acquisitions and c) any expected type of motion in clinical setting. The results have demonstrated both feasibility as well as ability to recover motion-degraded resolution without noise amplification in both dynamic and parametric PET images.

We have evaluated our method on simulated whole-body PET dynamic datasets with real human voluntary body motion and quantitative levels of noise in order to demonstrate the potential of the algorithm under highly challenging clinical conditions. Despite the high levels of noise, sparse time sampling and irregularity of intra- and inter-frame non-rigid bulk motions, the algorithm is able to successfully recover the major resolution components of all 6 original PET frames without further noise amplification. In addition, our method significantly enhanced the resolution of whole-body Patlak images, where the impact of motion was more evident, mainly due to inter-frame bulk motion. Therefore, we expect even better resolution recovery for less challenging acquisitions.

The proposed generalized RL-MCIR methods do not require gated acquisitions and, thus, can also be applied to studies where motion freezing through gating is challenging (dynamic short frames or highly irregular motion). Moreover,

as they do not rely on multiple gates, RL-MCIR algorithms are more computationally efficient than gated MCIR schemes. In addition, the former can potentially complement the latter with intra-gate motion compensation features as well.

The current study focuses mainly on motion compensation through the novel concept of nested RL deconvolution within ML-EM PET reconstruction, assuming motion tracking is accurate. Furthermore, both integrated and nested RL-MCIR methods are expected to converge to the same global ML solution. However, particularly in the presence of high noise, nested RL-MCIR converges at earlier iterations, before the noise is significantly amplified, thus, resulting in potentially higher contrast-to-noise ratios and faster computation.

ACKNOWLEDGMENT

This work was supported by the Swiss National Science Foundation under grant SNSF 31003A-149957. In addition, Dr. Karakatsanis and Dr. Tsoumpas were supported by two short-term scientific missions from EU COST action TD1007.

REFERENCES

- [1] N.A. Karakatsanis, M.A. Lodge, A.K. Tahari, Y. Zhou, R.L. Wahl and A. Rahmim, "Dynamic whole-body PET parametric imaging: I. Concept, acquisition protocol optimization and clinical application," *Phys. Med. Biol.* 58(20), pp. 7391-7418, 2013
- [2] N.A. Karakatsanis, M.A. Lodge, Y. Zhou, R.L. Wahl and A. Rahmim, "Dynamic whole-body PET parametric imaging: II. Task-oriented statistical estimation," *Phys. Med. Biol.* 58(20), pp. 7419-7445, 2013
- [3] A. Rahmim, J. Tang, and H. Zaidi, "Four-dimensional image reconstruction strategies in cardiac-gated and respiratory-gated PET imaging," *PET Clinics*, 8(1), pp. 51-67, 2013
- [4] C. Tsoumpas et al., "The effect of regularization in motion compensated PET image reconstruction: a realistic numerical 4D simulation study," *Phys. Med. Biol.* 58(6), 1759-1773, 2013
- [5] C. Kolbitsch, C. Prieto, C. Tsoumpas and T. Schaeffter, "A 3D MR-acquisition scheme for nonrigid bulk motion correction in simultaneous PET-MR," *Med Phys*, 41(8), 082304, 2014
- [6] K. Thielemans et al., "STIR: software for tomographic image reconstruction release 2," *Phys Med Biol*, vol. 57(4) pp.867-883, 2012
- [7] C. Buerger, T. Schaeffter and A.P. King, "Hierarchical adaptive local affine registration for fast and robust respiratory motion estimation," *Medical Image Analysis*, 15(4), pp. 551-564, 2011
- [8] K. Lange, D.R. Hunter and I. Yang, "Optimization transfer using surrogate objective functions," *Journal of Computational and Graphical Statistics*, 9(1), pp.1-20, 2000
- [9] N. Raghunath et al. "Motion correction of PET brain images through deconvolution: II. practical implementation and algorithm optimization," *Phys Med Biol* 54(3), 813-829, 2009
- [10] H. Mohy-ud-Din, N.A. Karakatsanis, M.R. Ay, C.J. Endres, D.F. Wong, and A. Rahmim, "Generalized inter-frame and intra-frame motion correction in PET imaging - a simulation study," *IEEE Nucl. Science Symp. & Med. Imag. Conf.*, pp. 3858-3862, 2011
- [11] N. A. Karakatsanis, et al., "Dynamic Multi-Bed FDG PET Imaging: Feasibility and Optimization", *IEEE Nucl. Sc. Symp. & Med. Imag. Conf.*, pp3863-3871, 2011
- [12] W.P. Segars, G. Sturgeon, S. Mendonca, J. Grimes, and B.M.W. Tsui, "4D XCAT phantom for multimodality imaging research," *Med Phys*,37(9), pp. 4902-4915, 2010
- [13] A. Könik et al., "Digital anthropomorphic phantoms of non-rigid human respiratory and voluntary body motion for investigating motion correction in emission imaging," *Phys.Med.Biol.* 59(14), pp.3669, 2014.